RESEARCH ARTICLE

High-Sensitivity Visualization of Ultrafast Carrier Diffusion by Wide-Field Holographic Microscopy

Martin Hörmann[1†], Federico Visentin[1†], Andrea Zanetta[2], Johann Osmond[3], Giulia Grancini[2], Niek F. van Hulst[3,4], Matz Liebel[3‡], Giulio Cerullo[1,5], and Franco V. A. Camargo[5*]

[1]Dipartimento di Fisica, Politecnico di Milano, Piazza L. da Vinci 32, 20133 Milano, Italy. [2]Department of Chemistry and INSTM, University of Pavia, Via T. Taramelli 14, 27100 Pavia, Italy. [3]ICFO - Institut de Ciencies Fotoniques, The Barcelona Institute of Science and Technology, 08860 Castelldefels, Barcelona, Spain. [4]ICREA - Institució Catalana de Recerca i Estudis Avançats, Passeig Lluís Companys 23, 08010 Barcelona, Spain. [5]IFN-CNR, Piazza L. da Vinci 32, 20133 Milano, Italy.

*Address correspondence to: franco.camargo@cnr.it
†These authors contributed equally to this work.
‡Present address: Department of Physics and Astronomy, Vrije Universiteit Amsterdam, De Boelelaan 1081, 1081 HV Amsterdam, The Netherlands.

Ultrafast transient microscopy is a key tool to study the photophysical properties of materials in space and time, but current implementations are limited to $\approx$1-μm fields of view, offering no statistical information for heterogeneous samples. Recently, we demonstrated wide-field transient imaging based on multiplexed off-axis holography. Here, we perform ultrafast microscopy in parallel around a hundred diffraction-limited excitation spots over a $\approx$60-μm field of view, which not only automatically samples the photophysical heterogeneity of the sample over a large area but can also be used to obtain a 10-fold increase in signal-to-noise ratio by computing an average spot. We apply our microscope to study the carrier diffusion processes in methylammonium lead bromide perovskites. We observe strong diffusion due to the presence of hot carriers during the first picosecond and slower diffusion afterward. We also describe how many-body kinetics can be misleadingly interpreted as strong diffusion at high excitation densities, while at weak excitation, real diffusion is observed. Therefore, the vast increase in sensitivity offered by this technique benefits the study of carrier transport not only by reducing data acquisition times but also by enabling the measurement of the much smaller signals generated at low carrier densities.

Introduction

Characterization of charge carrier transport processes in inorganic, organic, and hybrid semiconductors is the key for the development of next-generation photovoltaic devices [1]. Carrier diffusion constants and lengths can be measured with various experimental techniques, such as photoluminescence (PL) quenching [2,3], Hall effect [4], ultrafast terahertz spectroscopy [5,6], transient grating [7,8], and microwave photoconductivity [9,10]. However, most of these approaches rely on observables indirectly related with the diffusion combined with a model, resulting in large discrepancies among their results [11]. On the other hand, time-resolved PL and transient absorption (TA) microscopy provide a direct way to image exciton and carrier diffusion in real space and real time. While PL has temporal resolution limited to the picosecond time scale and is sensitive to bright excited states only, TA microscopy enables the observation of ultrafast diffusion phenomena down to the femtosecond time scale and is also sensitive to nonemitting states.

State-of-the-art TA microscopes used to study carrier diffusion in organic and inorganic materials all rely on photoexcitation of a single diffraction-limited spot and probe the response of the sample around that spot either with a wide-field or with a scanning probe configuration. Since only a spatially confined area of the sample is excited, the dynamic spread of the TA signal around this spot is indicative of diffusion of the photogenerated carriers. However, because of the limited frame rates of multipixel camera sensors, most TA microscopes use confocal designs, exploiting single-pixel detectors and fast raster scanning [12–17]. Wide-field cameras have been used only with low-repetition-rate (<1 kHz) laser pulses [18] or by compromising shot-noise limited detection and acquiring images at a frame rate much lower than the laser repetition rate [19–24]. This limits the sample area that one can measure within reasonable times to a few squared micrometers and prevents one from capturing large-scale heterogeneities of the sample in a single image. To determine the average properties of the material, it is therefore often necessary to average data from measurements sequentially performed on different parts of the sample

[16,17,22,24], substantially increasing data acquisition times and leaving open the question of how representative of the entire sample the few measured spots are.

Recently, we have introduced an ultrafast holographic transient (UHT) microscope, which overcomes the camera frame-rate limitation by exploiting off-axis holography to decouple the signal demodulation frequency from the frame rate of the camera and, thus, enabling shot-noise limited, large field-of-view transient microscopy [25]. Here, we exploit the wide field of view provided by the UHT microscope to photoexcite the sample in parallel with a hundred diffraction-limited spots, yielding diffusion data around all of them in a single measurement. This approach presents 2 major advantages: (a) The carrier diffusion properties can be characterized for hundreds of spots simultaneously covering a large area, experimentally assessing the effect of spatial heterogeneity on the photophysics of the sample; (b) when only the average behavior is desired, the signals from different spots can be averaged to increase the signal-to-noise ratio (SNR).

Materials and Methods

Experimental design

Figure 1A shows a sketch of the experimental setup, the holographic aspects of which have been described in detail before [25,26]. Briefly, it consists of a wide-field TA microscope in which the probe pulse is made to interfere on the camera with 2 reference pulses in a diagonally off-axis multiplexed holography configuration [27]. The references are modulated synchronously with the pump according to the scheme of Fig. 1B: One reference is present only when the pump illuminates the sample, while the other is present only when the pump is blocked. In the spatial 2-dimensional (2D) Fourier transform of the image, the interference terms are displaced from zero momentum (DC), a direct result of the angle between the wave vectors of the reference and image waves (see Fig. S1). The interference term for each wave can be cropped and shifted to zero, after which an inverse Fourier transform reconstructs the amplitude and phase of the original image. Since each reference is associated with either the pumped or the unpumped sample, a pixel-by-pixel subtraction of these images corresponds to the TA image of the whole field of view. The simultaneous

acquisition of pumped and unpumped sample images allows to decouple modulation frequency and camera frame rate, with only the latter being limited by the camera's technology. Thus, the UHT microscope acts as an all-optical wide-field digital lock-in camera, with the advantage of allowing a direct demodulation of the entire 2D image in a single exposure. As a consequence of the high modulation frequency, the resulting TA images show shot-noise limited signal fluctuations [25]. Further, the holographic nature of the technique recovers both amplitude and phase of the signal, which allows postacquisition digital processing of the image, such as computational focusing through the angular spectrum method [28] and hence recording out-of-focus TA dynamics of the sample [26].

We create the aforementioned excitation pattern by propagating the pump beam through an array of small apertures of 10 μm in diameter spread in a hexagonal lattice of a characteristic length of 80 μm on a 200-nm-thick gold foil (inset of Fig. 1A). A relay imaging system composed of the objective lens and an additional lens images the pinhole array into the sample plane and further allows freely adjusting the excitation spot size. Since each hole acts as a small aperture, diffraction effects must be considered, which, in the case of a periodic grating, manifest themselves in the form of the Talbot effect (see the Supplementary Materials for details) [29–32]. In this work, a demagnification of 13.89 is chosen to obtain ≈100 Gaussian spots with 756-nm full width at half maximum (FWHM) diameter spread across the 60-μm field of view (Fig. 1C).

Setup description

Spectrally tunable pulses are generated by a home-built non-collinear optical parametric amplifier, pumped by a 2-kHz, 100-fs amplified Ti:Sapphire laser system (Libra 2, Coherent), as described previously [33]. The 400-nm pump pulse is directly obtained by frequency doubling the laser output and modulated at 1 kHz with a mechanical chopper (MC2000B, Thorlabs). A 90:10 beam splitter generates the probe and reference beams from the noncollinear optical parametric amplifier output. The probe is focused onto the sample with a $f = 200$-mm achromatic lens (AC-254-200-A, Thorlabs) to cover the whole field of view. A microscope objective (numerical aperture = 0.8; UPLXAPO20X, Olympus) images the sample onto a complementary metal-oxide semiconductor camera (Basler ace acA720-520um, Basler AG)
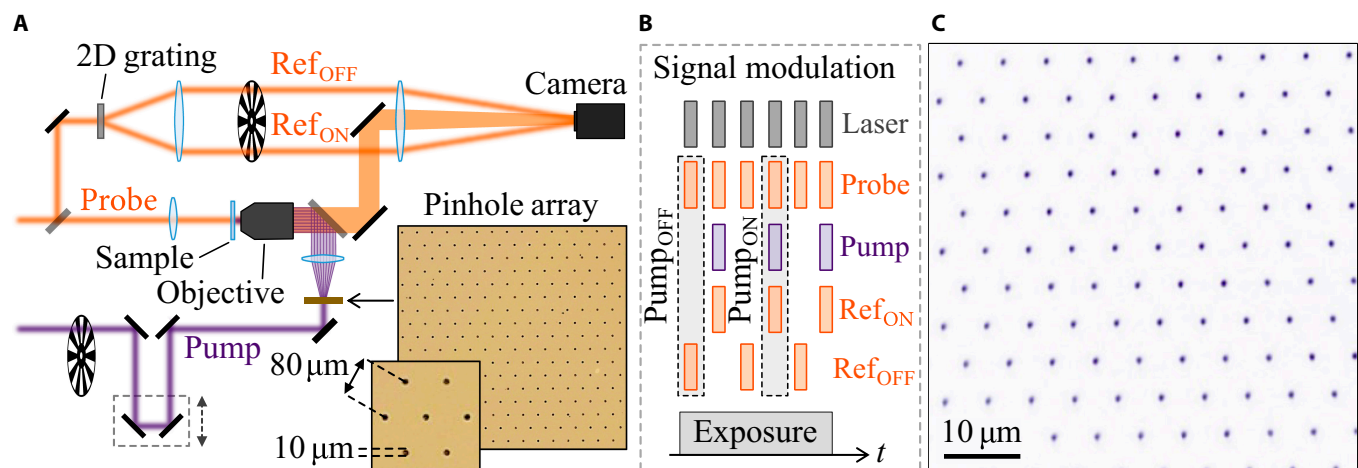
Fig. 1. UHT experimental setup. (A) Schematic of the experimental setup. Inset: Image of the pinhole array. (B) Signal modulation. (C) Image of the pump illumination pattern obtained using a mirror at the sample position.

with a nominal magnification of ×67. Holograms (540 pixels × 540 pixels) are recorded at 166 fps with an exposure time of 5.6 ms. To allow holographic imaging with femtosecond pulses [34], the reference beam is relay-imaged onto the same camera, and the 2 reference pulses are obtained by placing a 2D diffraction grating (MS-561-600-Y-A, HOLO/OR) in the conjugate image plane to allow interference over the entire camera chip. Two of the first diffraction orders are spatially selected and are modulated at 1 kHz with a second mechanical chopper to achieve the modulation scheme illustrated in Fig. 1B. The time delay between probe and reference pulses is adjusted by maximizing the interference fringe contrast with a mechanical delay line. The variable time delays between pump and probe pulses are obtained by means of a computer-controlled translation stage (M-531.PD1, Physik Instrumente).

Sample preparation

$MAPbBr_3$ hybrid perovskite samples were analysed in form of thin films deposited on glass substrates by solution-based spin coating process. The glass substrates (2 cm × 2 cm) were sequentially cleaned in soap water (Hellmanex III, Hellma), acetone and 2-propanol by ultrasonication for 15 min. Then, a 10-min O_2 plasma cleaning treatment was done to improve their wettability. The $MAPbBr_3$ solution was prepared by mixing MABr (methylammonium bromide, Greatcell) and $PbBr_2$ (lead bromide, 99.99%, TCI America) powders in a 1:1 stoichiometric ratio. The powders were then dissolved in a 4:1 DMF:DMSO vol/vol solvent mixture [DMF (N,N′-dimethylformamide), 99.8%, Sigma-Aldrich; DMSO (dimethyl sulfoxide), 99.8%, anhydrous, Sigma-Aldrich] and stirred at room temperature for 2 h until complete dissolution. The so-formed solution was then deposited on top of the glass substrates by spin coating at 5,000 rpm for 35 s with an acceleration of about 1,500 rpm/s.

After 6 s from the starting of the process, 150 μl of chlorobenzene (99.8%, anhydrous, Sigma-Aldrich) was dripped on the spinning substrates as solvent quenching step, to favor the crystallization of the polycrystalline perovskite thin film. Finally, the films were annealed for 30 min at 100 °C.

Pinhole array fabrication

AZ 5214 E photoresist was spin-coated on a previously cleaned microscope glass substrate and baked for 90 s at 100 °C. The design of the hexagonal lattice of Fig. 1A (inset) was exposed with a maskless aligner (MLA 150, Heidelberg Instruments) at a fluence of 100 mJ/cm^2 with an exposure wavelength of 375 nm, developed in AZ 726 MIF for 1 min, and rinsed in deionized water. Subsequently, a 2-nm Ti adhesion layer and 200-nm Au film were deposited on the substrate by thermal evaporation (Lab 18 Thin Film Deposition System, Kurt J. Lesker Co.). The result was left for lift-off in acetone for one night and rinsed in 2-propanol.

Results and Discussion

To validate the concept, we perform wide-field TA microscopy with ≈150-fs temporal resolution on thin films of the methylammonium lead bromide ($MAPbBr_3$) perovskites, photoexcited above the bandgap at λ = 400 nm and probed at their band edge at λ = 525 nm with $\Delta\lambda_{FWHM}$ = 7-nm probe pulse bandwidth (Fig. S3). Because of the low exciton binding energy of this material, we are essentially probing free charge carriers [35,36]. Figure 2A shows a typical TA image obtained with this technique, which is equivalent to performing a hundred of confocal TA microscopy experiments in parallel. For each spot, we can study the temporal evolution of the TA image (Fig. 2B): The positive differential transmission ($\Delta T/T$) comes from the
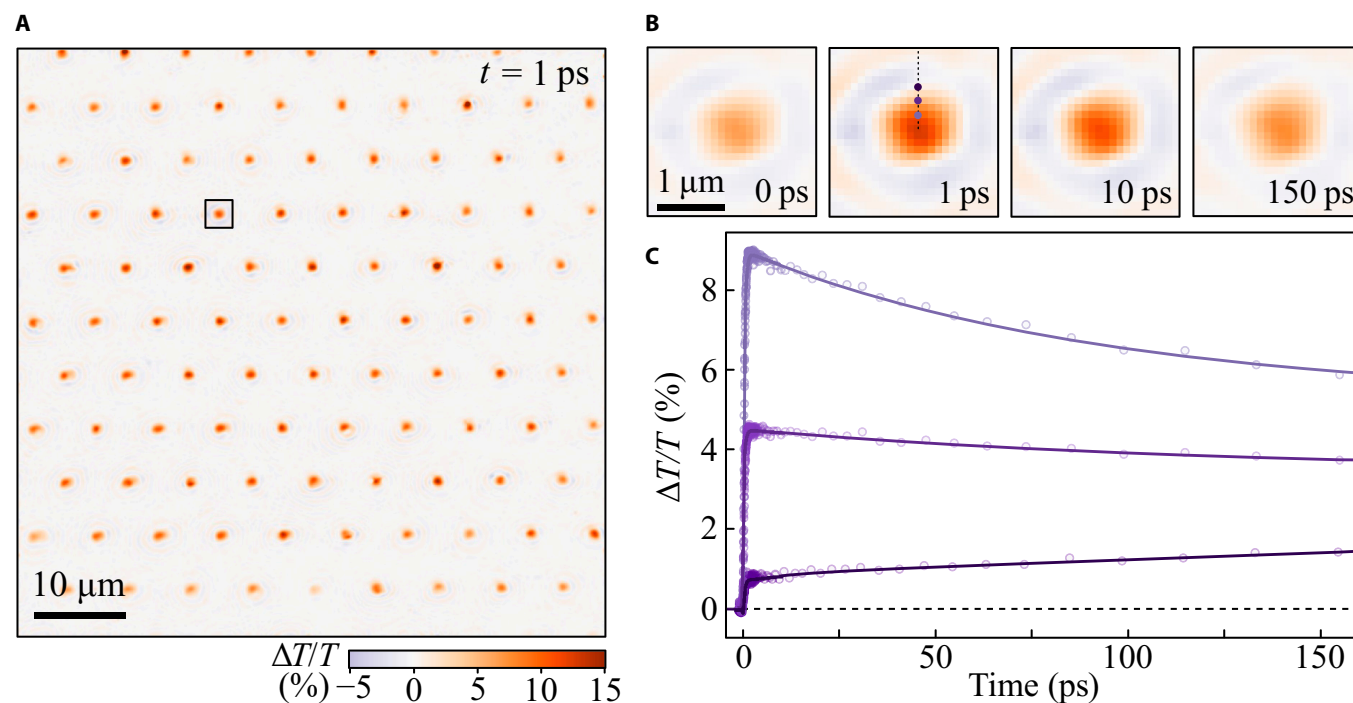

Fig. 2. Wide-field TA microscopy of $MAPbBr_3$ thin films. (A) TA image of a thin film of $MAPbBr_3$ probed at 525 nm at 1-ps delay. (B) Temporal evolution of a representative spot indicated by the square in (A). (C) TA kinetics of 3 pixels corresponding to different distances from the center of the excited spot. The full lines are the result of a multiexponential fit to help visualize the data.

photobleaching of the band edge transition, and the expansion of the spot size at longer times is due to diffusion of charge carriers. Carrier diffusion can be also observed in the TA kinetics for each pixel (Fig. 2C), showing increasing signals at longer times far from the spot's center.

To extract the charge carrier diffusion properties, we perform a Gaussian fit of the spot in the TA image and extract the diffusion coefficient D from the mean square deviation (MSD) as [11,14,19,20]:

$$\text{MSD} \equiv \sigma^2(t) - \sigma^2(0) = 2Dt \qquad (1)$$

where $\sigma^2(t)$ is the variance of the Gaussian distribution at time t. To analyze the data, we isolate 5-µm × 5-µm areas around each spot, and 2 different approaches are possible: (a) first, fit the spots individually and then compute the average variance; or (b) first, calculate the average spot and then fit it to extract its variance. With the first approach, we obtain both the average variance and the variance for each spot, allowing us to visualize how the diffusion properties are distributed across the photo-excited spots. On the other hand, averaging the spots allows us to significantly improve the SNR by a factor of the square root of the number of spots, rendering smaller signals detectable with a significant reduction of measurement times, which is convenient for the 2-kHz repetition rate of the laser system used.

To demonstrate the SNR improvement by averaging multiple spots, we analyze the noise at a negative delay time, where the signal is zero and only noise is present, and compare the fluctuations of single spots with the average spot at the same delay. Figure 3A to C shows maps around a single spot at a negative delay as the total acquisition time for the full image is increased from 10 to 84 s, while Fig. 3D to F shows the corresponding maps if the average of 80 spots is taken. By averaging 80 spots, we increase the SNR by a factor of $\sqrt{80}$, which is reflected in Fig. 3D showing less noise than Fig. 3C despite the acquisition time being reduced by almost one order of magnitude.

Having validated our technique, we apply it to TA microscopy experiments on a polycrystalline thin film of MAPbBr$_3$, whose diffusion properties have been described in detail before [37–41]. The experiments are performed at room temperature for 2 different excitation fluence regimes, namely, $F = 84$ and 7.5 µJ/cm^2, corresponding to carrier densities of 2.75×10^{18} and 2.45×10^{17} cm^{-3}, respectively (see the Supplementary Materials for fluence characterization and carrier density estimation). The spots are first averaged, and the average spot is fitted with a 2D Gaussian function to extract a diffusion coefficient as described previously.

Figure 4A and B shows the time evolution of the average spot for both fluences. While the low-fluence transient spot size in Fig. 4B is comparable to that obtained by directly imaging the excitation spot at the sample position (Fig. 1C), the high-fluence images show much larger spots, reflecting a saturation of the TA signal near the peak due to the high photon flux. Indeed, a power increase by a factor of 11 results in a signal increase by only a factor of ~4 (Fig. 4A and B), showing that the high fluence is well inside the saturation regime. Figure 4C and D shows the variance of the charge carrier distribution obtained by fitting the average spot with the 2D Gaussian function. Both fluences show a rapid increase in the variance in the first picosecond, due to hot carrier diffusion with a coefficient of the order of hundreds of square centimeters per second, followed by a slower diffusion of cold carriers, as already observed in similar samples [14]. The same diffusion behavior has also been observed for hot electrons in gold thin films [42]. The fast diffusion, which
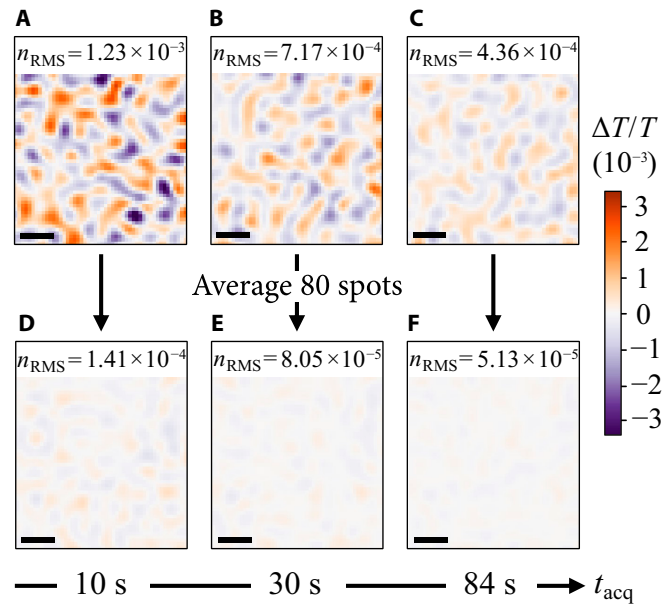

Fig. 3. Noise reduction by averaging multiple spots for different acquisition times. (A to C) Root mean square noise n_{RMS} around a 50-pixel × 50-pixel area at a negative pump–probe delay. The acquisition time refers to the total time from several individual frames with 5.6-ms integration each. (D to F) Noise of the average of 80 such regions at negative pump–probe delay. Scale bars, 1 µm. The SNR improvement as a function of the data acquisition time is summarized in Fig. S7.

occurs in a quasi-ballistic regime, correlates perfectly with the cooling time of hot carriers and was shown to be absent after excitation without excess energy [14]. Moreover, ballistic ultrafast, sub-100-fs, diffusion has also been reported, which may lead to a larger distribution even around time zero (see Fig. S8) [21,22]. Carrier–carrier interactions dominate the photophysical behavior in such ultrashort time scales, so experiments with higher temporal resolution are required to address it [43]. The diffusion coefficient at later times is computed using Eq. 1 by fitting the points from 5 ps, where effects of the rapid initial expansion are no longer present. This yields $D = 2.38$ cm^2/s for $F = 84$ µJ/cm^2 and $D = 0.20$ cm^2/s for $F = 7.5$ µJ/cm^2. Previously reported carrier diffusion coefficients of MAPbBr$_3$ fall in the range of $D = 0.16$ to 1.5 cm^2/s, measured with time-resolved PL microscopy [37], transient grating spectroscopy [38,39], transient reflectivity spectroscopy [40], and microscopy [41], with the variability attributed to differences in defect density and grain size between the samples [11,41]. The diffusion coefficient that we obtain with low-fluence excitation measurement falls within the lower boundaries of this range, while the one obtained at high fluences, which we name $D_{apparent}$, significantly exceeds reported values, suggesting that many-body interactions are responsible for the difference and more complex models have to be introduced to extract the true value of D under such conditions [44]. Indeed, moderately high fluences are associated to a substantial amount of Auger recombination (see Fig. S6) [45,46]. The nonlinear dependence of the Auger process on the density of excitons leads to a faster $\Delta T/T$ decay for the central part of the spot, in which the excitation density is higher because of the Gaussian spatial profile of the pump pulse, resulting in apparent broadening of the distribution, as already reported in other works [18,24]. Since typical excitation densities used in TA microscopy are much larger than those associated with natural sunlight illumination, care must be taken to obtain the diffusion
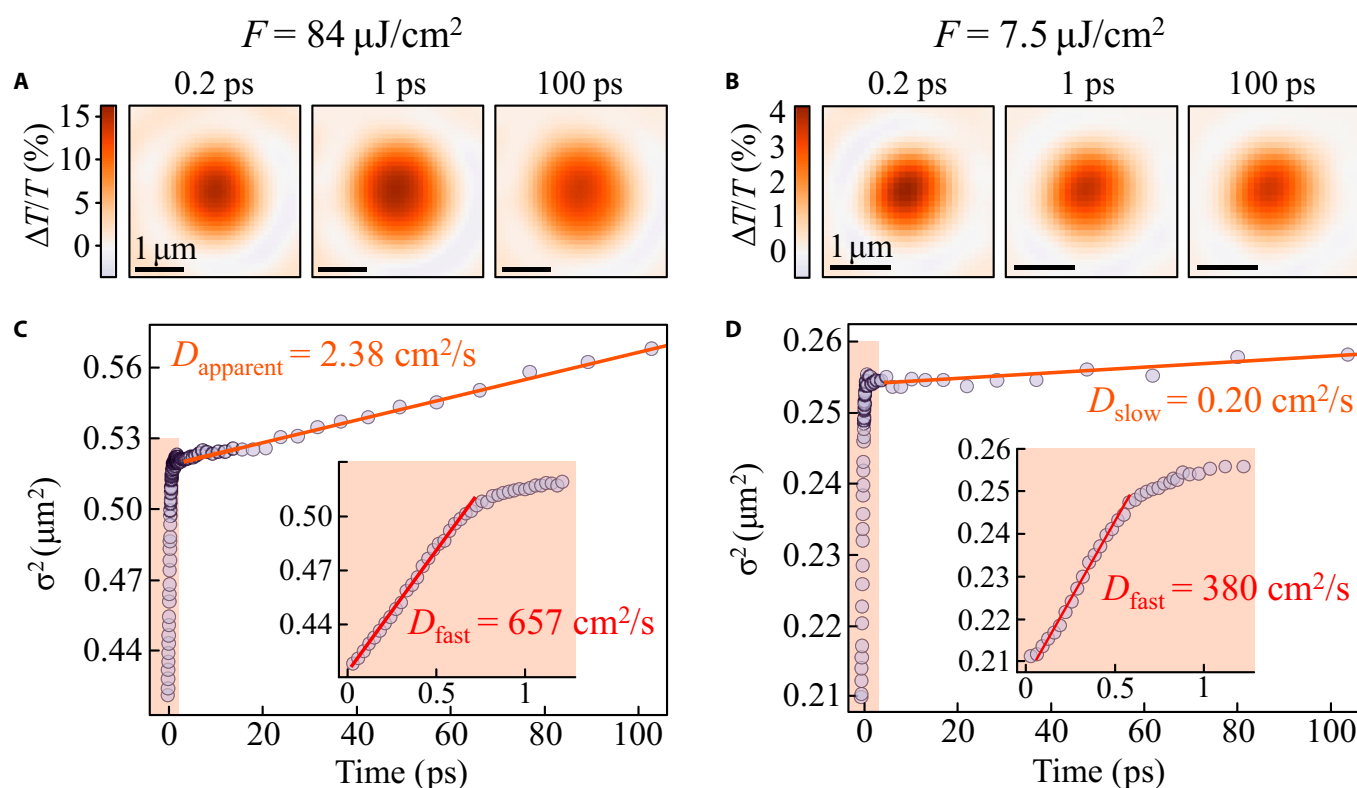
Fig. 4. MAPbBr$_3$ average diffusion properties. (A and C) $F = 84$ μJ/cm^2. (B and D) $F = 7.5$ μJ/cm^2. (A and B) Temporal evolution of the average spot over 100-ps time scale. Scale bars, 1 μm. (C and D) Variance of the average spot versus time and extracted diffusion coefficient. Inset: Zoom of the first picosecond. D_{fast} describes the fast diffusion of hot carriers that cool down to a value D_{slow} in few picoseconds, while the value $D_{apparent}$ observed in (C) is the result of many-body interactions occurring at high excitation densities that cannot be captured by a linear model considering only carrier diffusion.

coefficient in a fluence regime below the threshold for many-body effects. Averaging the spots as presented here is a powerful option in this sense, since we have demonstrated the capability of our wide-field TA microscope to reach low levels of noise with short measurement times, even with a low-repetition-rate (2 kHz) laser.

Conclusion

In summary, we have presented a new ultrafast microscopy technique that simultaneously acquires transient signals of 100 diffraction limited spots covering a sample area of ≈60 μm × 60 μm. This expansion of the spatial sampling by 2 orders of magnitude compared to current techniques is enabled by the all-optical lock-in camera concept, where off-axis holography with 2 reference waves modulated synchronously with the pump is used to encode pump$_{ON}$ and pump$_{OFF}$ images in k-space [25]. This key step decouples the camera frame rate from the signal demodulation rate, allowing shot-noise limited detection of the transient signals even when using camera frame rates much lower than the laser repetition rate, which was the limiting factor preventing wide fields of view to be obtained in ultrafast TA microscopy. We demonstrate how to profit from this large field of view using a pinhole array to create a structured photoexcitation pattern at the sample position that consists of around 100 diffraction limited spots. As a result, transient imaging at and around all these spots can be obtained in a single measurement. The data can be analyzed spot by spot to obtain statistics, or the individual spots can be averaged before the analysis. The latter option is particularly attractive

in the context of studying the photophysics of new photovoltaic materials, as it offers a route to obtain high-quality data of low signals, allowing lower excitation carrier densities to be used to avoid spurious many-body kinetics [47–49] that are irrelevant under natural sunlight excitation. Finally, we note that the 20× objective used in this work has a numerical aperture of 0.8 with a field number of 26.5. Hence, it is capable of imaging a 1.3-mm field of view if a top-end camera with a sufficient number of pixels is used, which would enable us to achieve more than 10^4 diffraction-limited excitation spots in a single measurement. Work in this direction is currently in progress.

Acknowledgments

Data Availability

The data reported in this article are freely available upon request to the authors.

Supplementary Materials

Ultrafast holographic transient microscopy
Optical characterization of MAPbBr$_3$ thin films
Fluence characterization
Carrier densities
Ultrafast ballistic diffusion
SNR improvement by averaging multiple spots
Talbot effect
Fig. S1. Holographic recording and image processing.
Fig. S2. Optical microscope image of a thin film of MAPbBr$_3$.
Fig. S3. Static absorption spectrum of a thin film of MAPbBr$_3$, pump, and probe spectra.
Fig. S4. TA spectroscopy of a thin film of MAPbBr$_3$.
Fig. S5. 2D Gaussian fit of the average pump spot of Fig. 1C.
Fig. S6. Fluence-dependent TA kinetics of a thin film of MAPbBr$_3$.
Fig. S7. SNR improvement by averaging 80 spots versus acquisition time.
Fig. S8. Ultrafast ballistic diffusion.

References

1. Li C, Wang A, Deng X, Wang S, Yuan Y, Ding L, Hao F. Insights into ultrafast carrier dynamics in perovskite thin films and solar cells. *ACS Photonics*. 2020;7:1893–1907.
2. Stranks SD, Eperon GE, Grancini G, Menelaou C, Alcocer MJP, Leijtens T, Herz LM, Petrozza A, Snaith HJ. Electron-hole diffusion lengths exceeding 1 micrometer in an organometal trihalide perovskite absorber. *Science*. 2013;342:341–344.
3. Gong X, Huang Z, Sabatini R, Tan C-S, Bappi G, Walters G, Proppe A, Saidaminov MI, Voznyy O, Kelley SO, et al. Contactless measurements of photocarrier transport properties in perovskite single crystals. *Nat Commun*. 2019;10:1591.
4. Yi HT, Wu X, Zhu X, Podzorov V. Intrinsic charge transport across phase transitions in hybrid organo-inorganic perovskites. *Adv Mater*. 2016;28:6509–6514.
5. Wehrenfennig C, Eperon GE, Johnston MB, Snaith HJ, Herz LM. High charge carrier mobilities and lifetimes in organolead trihalide perovskites. *Adv Mater*. 2013;26:1584–1589.
6. Wehrenfennig C, Liu M, Snaith HJ, Johnston MB, Herz LM. Charge-carrier dynamics in vapour-deposited films of the organolead halide perovskite CH3NH3PbI3-xClx. *Energy Environ Sci*. 2014;7:2269–2275.
7. Gedik N, Orenstein J, Liang R, Bonn DA, Hardy WN. Diffusion of nonequilibrium quasi-particles in a cuprate superconductor. *Science*. 2003;300:1410–1412.
8. Kuhn H, Wagner J, Han S, Bernhardt R, Gao Y, Xiao L, Zhu J, Loosdrecht PHM. Excitonic transport and intervalley scattering dynamics in large-size exfoliated MoSe$_2$ monolayer investigated by heterodyned transient grating spectroscopy. *Laser Photonics Rev*. 2020;14:2000029.
9. Ponseca CS Jr, Savenije TJ, Abdellah M, Zheng K, Yartsev A, Pascher T, Harlang T, Chabera P, Pullerits T, Stepanov A, et al. Organometal halide perovskite solar cell materials rationalized: Ultrafast charge generation, high and microsecond-long balanced mobilities, and slow recombination. *J Am Chem Soc*. 2014;136:5189–5192.
10. Savenije TJ, Ponseca CS, Kunneman L, Abdellah M, Zheng K, Tian Y, Zhu Q, Canton SE, Scheblykin IG, Pullerits T, et al. Thermally activated exciton dissociation and recombination control the carrier dynamics in organometal halide perovskite. *J Phys Chem Lett*. 2014;5:2189–2194.
11. Deng S, Blach DD, Jin L, Huang L. Imaging carrier dynamics and transport in hybrid perovskites with transient absorption microscopy. *Adv Energy Mater*. 2020;10:1903781.
12. Polli D, Grancini G, Clark J, Celebrano M, Virgili T, Cerullo G, Lanzani G. Nanoscale imaging of the interface dynamics in polymer blends by femtosecond pump-probe confocal microscopy. *Adv Mater*. 2010;22:3048–3051.
13. Grancini G, Polli D, Fazzi D, Cabanillas-Gonzalez J, Cerullo G, Lanzani G. Transient absorption imaging of P3HT:PCBM photovoltaic blend: Evidence for interfacial charge transfer state. *J Phys Chem Lett*. 2011;2:1099–1105.
14. Guo Z, Wan Y, Yang M, Snaider J, Zhu K, Huang L. Long-range hot-carrier transport in hybrid perovskites visualized by ultrafast microscopy. *Science*. 2017;356:59–62.
15. Piland G, Grumstrup EM. High-repetition rate broadband pump–probe microscopy. *J Phys Chem A*. 2019;123:8709–8716.
16. Hill AH, Smyser KE, Kennedy CL, Massaro ES, Grumstrup EM. Screened charge carrier transport in methylammonium lead iodide perovskite thin films. *J Phys Chem Lett*. 2017;8:948–953.
17. Kennedy CL, Hill AH, Massaro ES, Grumstrup EM. Ultrafast excited-state transport and decay dynamics in cesium lead mixed halide perovskites. *ACS Energy Lett*. 2017;2:1501–1506.
18. Guo Z, Zhou N, Williams OF, Hu J, You W, Moran AM. Imaging carrier diffusion in perovskites with a diffractive optic-based transient absorption microscope. *J Phys Chem C*. 2018;122:10650–10656.
19. Delor M, Weaver HL, Yu Q, Ginsberg NS. Imaging material functionality through three-dimensional nanoscale tracking of energy flow. *Nat Mater*. 2019;19:56–62.
20. Schnedermann C, Sung J, Pandya R, Verma SD, Chen RYS, Gauriot N, Bretscher HM, Kukura P, Rao A. Ultrafast tracking of exciton and charge carrier transport in optoelectronic materials on the nanometer scale. *J Phys Chem Lett*. 2019;10:6727–6733.
21. Sung J, Schnedermann C, Ni L, Sadhanala A, Chen RYS, Cho C, Priest L, Lim JM, Kim H-K, Monserrat B, et al. Long-range ballistic propagation of carriers in methylammonium lead iodide perovskite thin films. *Nat Phys*. 2019;16:171–176.
22. Sung J, Macpherson S, Rao A. Enhanced ballistic transport of charge carriers in alloyed and K-passivated alloyed perovskite thin films. *J Phys Chem Lett*. 2020;11:5402–5406.
23. Pandya R, Alvertis AM, Gu Q, Sung J, Legrand L, Kréher D, Barisien T, Chin AW, Schnedermann C, Rao A. Exciton diffusion in highly-ordered one dimensional conjugated polymers: Effects of back-bone torsion, electronic symmetry, phonons and annihilation. *J Phys Chem Lett*. 2021;12:3669–3678.
24. Sneyd AJ, Fukui T, Paleček D, Prodhan S, Wagner I, Zhang Y, Sung J, Collins SM, Slater TJA, Andaji-Garmaroudi Z, et al. Efficient energy transport in an organic semiconductor mediated by transient exciton delocalization. *Sci Adv*. 2021;7(32):eabh4232.

25. Liebel M, Camargo FVA, Cerullo G, van Hulst NF. Ultrafast transient holographic microscopy. *Nano Lett*. 2021;21:1666–1671.

26. Liebel M, Camargo FVA, Cerullo G, van Hulst NF. Widefield phototransient imaging for visualizing 3D motion of resonant particles in scattering environments. *Nanoscale*. 2022;14:3062–3068.

27. Dardikman G, Shaked NT. Is multiplexed off-axis holography for quantitative phase imaging more spatial bandwidth-efficient than on-axis holography? [Invited]. *J Opt Soc Am A*. 2018;36(2):A1–A11.

28. Goodman JW. *Introduction to Fourier optics*. New York: W.H. Freeman & Co Ltd; 2005.

29. Talbot HF. Facts relating to optical science. *Phil Mag*. 1836;9:1–4.

30. Rayleigh W. On copying diffraction gratings, and on some phenomena connected therewith. *Phyl Mag*. 1881;11:196–205.

31. Qu W, Liu L, Liu D, Luan Z, Xu N. The fractional talbot effect of two-dimensional array. *SPIE Proc*. 2005; 10.1117/12.612711.

32. Zhu L-W, Yin X, Hong Z, Guo C-S. Reciprocal vector theory for diffractive self-imaging. *J Opt Soc Am A*. 2007;25:203.

33. Manzoni C, Polli D, Cerullo G. Two-color pump-probe system broadly tunable over the visible and the near infrared with sub-30 fs temporal resolution. *Rev Sci Instrum*. 2006;77:023103.

34. Maznev AA, Crimmins TF, Nelson KA. How to make femtosecond pulses overlap. *Opt Lett*. 1998;23:1378–1380.

35. Lin Q, Armin A, Nagiri RCR, Burn PL, Meredith P. Electro-optics of perovskite solar cells. *Nat Photonics*. 2014;9:106–112.

36. Galkowski K, Mitioglu A, Miyata A, Plochocka P, Portugall O, Eperon GE, Wang JT-W, Stergiopoulos T, Stranks SD, Snaith HJ, et al. Determination of the exciton binding energy and effective masses for methylammonium and formamidinium lead tri-halide perovskite semiconductors. *Energy Environ Sci*. 2016;9:962–970.

37. Tian W, Zhao C, Leng J, Cui R, Jin S. Visualizing carrier diffusion in individual single-crystal organolead halide perovskite nanowires and nanoplates. *J Am Chem Soc*. 2015;137:12458–12461.

38. Ščajev P, Aleksiejūnas R, Miasojedovas S, Nargelas S, Inoue M, Qin C, Matsushima T, Adachi C, Juršėnas S, Aleksiejūnas R, et al. Two regimes of carrier diffusion in vapor-deposited lead-halide perovskites. *J Phys Chem C*. 2017;121:21600–21609.

39. Ščajev P, Miasojedovas S, Juršėnas S. A carrier density dependent diffusion coefficient, recombination rate and diffusion length in $MAPbI_3$ and $MAPbBr_3$ crystals measured under one- and two-photon excitations. *J Mater Chem C*. 2020;8:10290–10301.

40. Yang Y, Yan Y, Yang M, Choi S, Zhu K, Luther JM, Beard MC. Low surface recombination velocity in solution-grown $CH_3NH_3PbBr_3$ perovskite single crystal. *Nat Commun*. 2015;6:7961.

41. Kennedy CL, Hill AH, Grumstrup EM. Screening links transport and recombination mechanisms in lead halide perovskites. *J Phys Chem C*. 2019;123:15827–15833.

42. Block A, Liebel M, Yu R, Spector M, Sivan Y, García de Abajo FJ, van Hulst NF. Tracking ultrafast hot-electron diffusion in space and time by ultrafast thermomodulation microscopy. *Sci Adv*. 2019;5(5):aav8965.

43. Richter JM, Branchi F, Camargo FVA, Zhao B, Friend RH, Cerullo G, Deschler F. Ultrafast carrier thermalization in lead iodide perovskite probed with two-dimensional electronic spectroscopy. *Nat Commun*. 2017;8:376.

44. deQuilettes DW, Brenes R, Laitz M, Motes BT, Glazov MM, Bulović V. Impact of photon recycling, grain boundaries, and nonlinear recombination on energy transport in semiconductors. *ACS Photonics*. 2021;9:110–122.

45. Delport G, Chehade G, Lédée F, Diab H, Milesi-Brault C, Trippé-Allard G, Even J, Lauret J-S, Deleporte E, Garrot D. Exciton–exciton annihilation in two-dimensional halide perovskites at room temperature. *J Phys Chem Lett*. 2019;10:5153–5159.

46. Pazos-Outón LM, Xiao TP, Yablonovitch E. Fundamental efficiency limit of lead iodide perovskite solar cells. *J Phys Chem Lett*. 2018;9:1703–1711.

47. Piris J, Dykstra TE, Bakulin AA, Loosdrecht PHM, Knulst W, Trinh MT, Schins JM, Siebbeles LDA. Photogeneration and ultrafast dynamics of excitons and charges in P3HT/PCBM blends. *J Phys Chem C*. 2009;113:14500–14506.

48. Bourelle SA, Shivanna R, Camargo FVA, Ghosh S, Gillett AJ, Senanayak SP, Feldmann S, Eyre L, Ashoka A, van de Goor TWJ, et al. How exciton interactions control spin-depolarization in layered hybrid perovskites. *Nano Lett*. 2020;20:5678–5685.

49. van Oort B, Roy LM, Xu P, Lu Y, Karcher D, Bock R, Croce R. Revisiting the role of xanthophylls in nonphotochemical quenching. *J Phys Chem Lett*. 2018;9:346–352.